Stainless steel wire mesh-supported ZnO for the catalytic photodegradation of methylene blue under ultraviolet irradiation

Tan T. Vu, Laura del Río, Teresa Valdés-Solís and Gregorio Marbán♣

Instituto Nacional del Carbón (INCAR-CSIC) – c/Francisco Pintado Fe 26, 33011-Oviedo (Spain). Tel. +34 985119090; Fax +34 985297662

Article published in Journal of Hazardous Materials, 246-247 (2013) 126-134

Abstract

The aim of this study was to assess the activity of catalysts formed by nanostructured zinc oxide supported on stainless steel wire mesh for the photocatalytic degradation of methylene blue under UV irradiation. Catalysts prepared by means of different low temperature synthesis methods, as described in a previous work (Vu et al., Mater. Res. Bull., 47 (2012) 1577-1586), were tested. A new activity parameter was introduced in order to compare the catalytic activity of the different catalysts. The best catalyst showed a catalytic activity higher than that of the reference material TiO2 P25 (Degussa-Evonik). This high activity is attributed to a higher quantum yield derived from the small particle length of the ZnO deposited on the wire mesh. The photocatalytic degradation kinetics of methylene blue fitted a potential model with n orders ranging from 0.5 to 6.9. Reaction orders over 1 were attributed to catalyst deactivation during the reaction resulting from the photocorrosion of ZnO.

Keywords: Photocatalysis; catalytic activity; ZnO; stainless steel mesh; deactivation

---

♣ Corresponding author: greca@incar.csic.es

1. Introduction

Around one million tons of synthetic organic dyes are produced every year for the textile, leather, paint, food, plastics and cosmetics industries. A sizeable fraction of this is lost during the industrial process in wastewaters which are usually discharged into rivers and seas. The decolouring and cleaning of these polluted effluents is essential for the environmental sustainability of the above-mentioned industries. Heterogeneous photocatalysis is one of the most attractive technologies for the decomposition of organic substances in wastewaters [1]. There are several materials with appropriate properties for acting as photocatalysts, such as TiO_2, ZnO, CdS, iron oxides, WO_3, ZnS, etc. Of these TiO_2 is the most widely used catalyst because it is relatively cheap and supplies photogenerated holes with great oxidative potential [2]. Zinc oxide shares many of the properties of TiO_2, including a similar bandgap. Due to the high demand for titanium in multiple applications the price of ZnO is now lower than that of TiO_2 [3]. Several studies claim that ZnO is even more active than TiO_2 and provides a higher quantum yield [4,5].

The use of ZnO catalysts in powder form implies a series of technical challenges, one of which is the separation of the particles from the reaction medium. Using a support for the photocatalysts maintains the dispersion of the particles and prevents sintering and agglomeration. Some supports also play an active role in the catalytic process by favouring charge separation (high electric conductivity supports) or the adsorption of reactants (highly porous supports). There are many reports in the literature of the direct synthesis of zinc oxide on different supports [6-11] such as ITO (indium tin oxide [9,10]), copper plates [11], silica, crystal or polyester films [10], polyethylene fibres [12], etc. The synthesis methods described in the literature [13] produce a wide variety of crystal morphologies, depending on the type of structure-directing agent used, e.g., hexamethylenetetramine, polyethylene glycol, polyethylene imine, etc. In general these

are low-temperature hydrothermal methods (below 100°C) sometimes followed by a calcination stage (350-450°C).

We recently used several of these procedures [7-11] to synthesize ZnO nanoparticles supported on stainless steel wire mesh [14]. Wire mesh-supported materials have recently been used as monolithic catalysts for different reactions (e.g. the preferential oxidation of CO [15], methanol decomposition [16] and N_2O decomposition [17]). In the present study the materials produced were tested for the photodegradation of methylene blue solutions under ultraviolet irradiation. The results were then compared with those achieved with commercial TiO_2 particles (Degussa-Evonik P25).

2. Experimental

2.1 Catalyst

All of the chemical reagents were of analytical grade and were not subjected to additional purification. The aqueous solutions were prepared with deionised water. The support was a stainless steel wire mesh [with a wire diameter of 30 μm and a screen opening of 40 μm] provided by CISA. Prior to being coated with ZnO, the mesh was washed with HNO_3 (4M) at 60°C for 4 hours and then with isopropyl alcohol in an ultrasonic bath for 10 minutes. The following reagents were employed: hexahydrated zinc nitrate (98%; Sigma-Aldrich), zinc chloride (Prolabo), dihydrated zinc acetate (Prolabo), polyethylene imine (PEI; MW=800; Sigma-Aldrich), hexamethylenetetramine (HMTA; >99.5%; Sigma-Aldrich), polyethylene glycol (PEG; MW=10,000; Sigma-Aldrich); aqueous ammonium hydroxide (20-30 vol.%; Sigma-Aldrich), absolute ethanol (96%; Panreac) and potassium hydroxide (>85%; Probus). The different synthesis procedures used with these reagents [7-11,18] are described in detail in [14]. Table 1 contains a list of all of the catalysts prepared in this

work together with the variables employed for each method of synthesis. The references used in this work are the same as those in [14].

The photocatalytic experiments were performed over aqueous solutions of monohydrated methylene blue (>96%; Riedel de Häen). Commercial TiO_2 particles (Degussa-Evonik P25) were used for comparison purposes.

2.2 Catalyst characterization

The morphology of the catalysts was studied by means of scanning electron microscopy (SEM, FEI Quanta FEG 650 model). Image analysis of the microphotographs was applied in order to evaluate the ZnO crystal dimensions (W=width, L=length, S=average separation between adjacent prisms; nm). With these parameters and the ZnO yield on a mass basis (Y, wt.%), the geometric surface area of ZnO (cm^2/g_{ZnO}) was evaluated by means of the following equation:

$$S_g = 3S_m \frac{W\left(L + \frac{\sqrt{3}}{8}W\right)\left(1 - \frac{Y}{100}\right)}{\left(S + W\right)^2} \qquad (1)$$

where S_m is the specific surface area of the clean mesh (135 cm^2/g). To derive this equation it was assumed that the ZnO crystals are hexagonal prisms that grow perpendicular to the substrate surface. Therefore, the application of this method to the samples with a flower-like prism arrangement introduced a high degree of uncertainty with respect to the geometric surface area value. This parameter, which in no case is equivalent to the specific surface area of the samples, should only be used to rank materials with different geometric surface areas. The X-ray diffraction (XRD) patterns of the catalysts were recorded on a Bruker D8 Advance instrument operating at 40 kV and 40 mA and using Cu Kα radiation (λ = 0.15406 nm). The crystal size values were estimated from the XRD pattern by means of Scherrer's equation (d_{XRD}). The relative

abundance of polar surfaces in the catalysts was evaluated from the ratio of the intensities of peak (101) to peak (002) (I_{101}/I_{002}) in the zincite XRD patterns. The values for all these structural characterisation parameters can be found in [14].

2.3 Photocatalytic tests

The photocatalytic methylene blue degradation experiments were carried out both on the supported catalysts (1×5 cm^2 strips weighing ~100 mg) and on the commercial TiO_2 particles (Degussa P25; 5-20 mg) in a 400 mL quartz beaker illuminated by two ring-type UV 22W lamps (Luzchem Ring-Illuminator) which generally emit radiation at 351 nm. The catalysts were immersed in a 60 mL aqueous solution of methylene blue, with an initial concentration of 10 mg/L. The reaction medium was magnetically stirred for 30 min under darkness to ensure adsorption/desorption equilibrium between the dye and the photocatalyst. Next the reactor was exposed to the UV lamps. Analytical samples were extracted for measurement after various reaction times, those with TiO_2 particles being centrifuged to remove the particles before analysis. The visible absorption peaks of the analyzed samples were recorded in the 400-800 nm range by means of a UV-Vis spectrometer (Shimadzu UV-2401PC). The true methylene blue concentration was obtained from the visible absorption spectra by means of a recently published deconvolution technique [19] that takes into account the contribution of reaction intermediates to the spectra. In order to compare the photocatalytic activities of the materials the following considerations were applied:

(i) the catalyst dosage ($C_C=w_C/V$, where w_c is the weight of the catalyst and V is the volume of the liquid) remains constant during the reaction for the TiO_2 particles, but increases slightly for the meshes, due to the regular removal of liquid samples for

analysis. Thus, the actual catalyst dosage at any time t can be estimated from the following equation:

$$C_C = \frac{w_C}{V_0 \left(1 - b \times t\right)} \tag{2}$$

where V_0 is the initial liquid volume and b is a constant that can be evaluated by linear regression;

(ii) the reaction rate can be expressed by the potential equation:

$$-\frac{dC_{MB}}{dt} = kC_C C_{MB}^n \tag{3}$$

where C_{MB} is the methylene blue concentration at any given time t, k is the reaction constant ($mg_{MB}^{1-n} \cdot mg_c^{-1} \cdot L^n \cdot min^{-1}$) and n is the apparent reaction order. Factor C_C is introduced to account for the known dependence of the reaction rate on the catalyst concentration in the absence of screening effects [20-24]. Therefore, under chemical control the reaction constant k should be independent of the catalyst concentration.

For n=1, equation (3) is coincident with the known Langmuir-Hinshelwood equation for diluted solutions [25]. The resolution of equation (3) under different circumstances gives equations (4) to (7) shown in Table 2. By fitting the concentration values from these equations with the experimental values of C_{MB} at different times, the values of k and n can be obtained. However, the comparison of catalytic activities cannot be performed with the values of k unless the values of n are identical. To overcome this problem, we used the following parameter to evaluate the intrinsic activity of the catalysts:

$$A_C = 1 / t_{0.5} C_{C,0} \tag{8}$$

where $t_{0.5}$ is the semiconversion time (min). Depending on the values of C_C and n, parameter A_C ($mg_c^{-1} \cdot L \cdot min^{-1}$) can be evaluated by any of the equations (9) to (12) listed in Table 2. On a ZnO or TiO_2 mass basis, subscript *C* in equations (1) to (12) becomes

Z; on a catalyst mass basis, subscript *C* becomes *MZ* (mesh plus ZnO). Parameter A_C (A_Z or A_{MZ}) allows the activities of the catalysts to be compared at the same initial methylene blue concentration. In principle parameter A_C is independent of the catalyst concentration. This is evident for the cases where the catalyst concentration does not vary during the reaction (equations (9) and (11)).

3. Results and discussion

The deconvolution technique described elsewhere [19] was applied in this work to obtain the true methylene blue concentration during the photodegradation experiments carried out with TiO_2 P25 and with the catalysts listed in Table 1. Figure 1 shows specific spectra corresponding to the samples extracted from the reaction media at different times using different stainless steel mesh-supported catalysts. The grey peaks (P7, P8 and P9) correspond to the intermediate compounds produced during the reaction, whereas the six black peaks correspond to methylene blue, of which P1 exhibits the highest absorbance at the mean wavelength [19]. All the fittings displayed are highly acceptable, as in the case of the other samples analysed in this work.

Figure 2 shows examples of the evolution of absorbance during the reaction for peaks in the visible region (P1: methylene blue, P7-P8-P9: intermediate compounds) corresponding to catalysts with different activities. As can be seen, the absorbances for peaks P7, P8 and P9 vary in a way one would expect for intermediate products, increasing at the beginning of the reaction and starting to decrease when the methylene blue concentration has fallen almost to zero. Especially noticeable is the significant contribution of the absorbances of the intermediate products to the total absorbance of the system, since this proves that it is necessary to use the deconvolution technique to evaluate the exact methylene blue concentration. Table 3 shows the Gaussian

parameters corresponding to the peaks of the intermediate products (P7, P8 and P9), averaged for all the photocatalytic experiments carried out with the mesh-supported catalysts and with the TiO_2 particles. Both the mean wavelengths (λ_i) and the standard deviations (σ_i) are very similar for both types of materials (the mesh-supported and TiO_2 catalysts) which suggests that the intermediate compounds formed in both cases are the same. These are azur A and azur B. Azur A is produced by the gradual demethylation of azur B, which in turn is produced by the demethylation of methylene blue [19].

In order to establish a basis for comparison, photodegradation experiments with commercial TiO_2 particles (P25 Degussa-Evonik) were previously performed. Figure 3 shows the variation of the methylene blue concentration with reaction time for different amount of TiO_2. The dashed lines represent the fitting of experimental points to equation (4) (first order kinetics). With the kinetic constants obtained from the fitting, A_Z activity values were evaluated by means of equation (9). The inset in Figure 3 shows a plot of the values of A_Z for the different catalyst weights. As can be observed, the intrinsic catalytic activity (A_Z) is independent of catalyst mass for values of mass equal to or below 10 mg. The decrease in catalytic activity for higher masses is typical of photocatalytic systems [20-24] and it is commonly attributed to a screening effect resulting from the catalyst particles being situated close to the irradiation source. However this effect is usually observed for catalyst concentrations of more than 1 g/L [21,23] whereas in Figure 3 the decrease in A_Z starts to occur at ~0.25 g/L. In our experiments no air was bubbled in the reaction vessel during the reaction, and therefore for higher TiO_2 masses the supply of oxygen from the atmosphere may become the controlling step, since this is known to occur with other processes, such as the photodegradation of phenol [26]. Therefore, in order to compare the activity of the catalysts prepared in this work with that of commercial TiO_2 the A_Z value for the lowest

TiO_2 mass (5.8×10^{-4} $mg^{-1}\cdot L\cdot min^{-1}$ as indicated in Figure 3) will be used. This value corresponds to the intrinsic (independent of mass) activity of TiO_2.

Figure 4 shows the results of methylene blue photodegradation obtained for the different mesh-supported catalysts tested in this work. Remarkable differences in catalytic activity between the catalysts can be appreciated. The dashed lines in Figure 4 represent the fitting of the experimental data to equation (7). This equation was used because the classical first order reaction equation (5) provided unacceptable fittings in most cases, whereas the potential equation (7) gave good fitting results (Figure 4). The kinetic parameters obtained (k and n) are shown in Table 4. In several cases the reaction order is clearly superior to 1, which could imply that catalytic deactivation has taken place during the reaction due to the photocorrosion of zinc oxide [27-29]. However, the existence of different values for the reaction order makes it impossible to compare the catalytic activities using the values of k. Therefore, in order to perform a strict comparison of catalytic activities we shall make use of the activity parameter, A_C (either on a ZnO mass basis, A_Z, or on a total catalyst mass basis, A_{MZ}) as defined by equation (8) and evaluated for the mesh-supported catalyst by equation (12) and for the TiO_2 particles by equation (9). The values of A_Z and A_{MZ} are presented in Table 4. For a better visualization of the data Figure 5 shows the values of A_Z and A_{MZ} corresponding to the different catalysts. As can be observed, the most active catalyst on a ZnO mass basis (A_Z) is S2-Ko. This displays an even higher activity than TiO_2. The next most active is S2-Feng. The other catalysts all have a much lower catalytic activity. However, when considering the total mass of the catalyst (including the inert metallic mesh) none of the catalysts developed here have an activity comparable to that of TiO_2. This drawback is offset by the advantages derived from using a supported catalyst.

The catalytic activity of mesh-supported catalysts depends *a priori* on several factors such as the presence of polar surfaces, the specific surface area of the active phase

(number of active centres), the geometric properties, etc. Figure 6 shows the plots corresponding to the variation of A_Z with the values of the different structural parameters of the catalysts. In spite of what other authors have suggested [30], the catalytic activity of the ZnO nanoparticles produced in this work bears, in principle, no apparent relation to the abundance of polar facets, expressed by the difractometric relation I_{101}/I_{002} (Figure 6). Neither the crystal size (d_{XRD}) nor the specific geometric surface (S_g) seem to follow any noticeable trend with catalytic activity. However, a certain relationship can be observed between the A_Z and ZnO yield values (i.e. the higher the load of ZnO in the catalyst, the lower the catalytic activity) and even more clearly between A_Z and the nanoparticle dimensions, especially the length of the prisms, which shows an inverse relation with the catalytic activity. Possibly the ultraviolet radiation is more appropriately distributed (a better quantum yield) through the mesh-supported catalysts with a lower ZnO yield (because there is less ZnO mass to penetrate through) and, especially, in the samples with thinner ZnO deposits (smaller nanoparticles). Two examples of thick (S2-Ko) and thin (S2-Xu) deposits can be seen in the SEM images displayed in Figure 7. It is known that the optical transmittance of zinc oxide deposits is favoured by a diminution of their thickness [31], as illustrated in the figure. The apparent relation between A_Z and the values of W and S (Figure 6) might be a consequence of the expected relation between these parameters and L. Thus, if the catalysts with lower values of L are disregarded (L<1500 nm), then the expected relationship between catalytic activity and the abundance of polar surface (I_{101}/I_{002}) [30] becomes evident, as can be seen in the inset of Figure 6.

Three catalysts were selected for stability tests: the two most active catalysts on a total mass basis (S2-Ko and S2-Chen-10) and a catalyst with a reaction order close to one (S2-Bai-C). The tests consisted of following the catalytic activity during consecutive batch reaction stages. Figure 8 shows the variation of A_Z with t_{UV} for all the catalysts.

This time value (t_{UV}) only includes the summation of the reaction times under ultraviolet irradiation. It does not take into consideration the adsorption stages under darkness. Each point in the plot stands for one reaction stage (120-150 min reaction). After each stage the catalyst was cleaned and dried for the next reaction stage. As can be observed, all three catalysts become deactivated to a lesser or greater degree after several reaction stages, the most stable being the least active catalyst (S2-Bai-C). The rate of deactivation can be modelled using a potential equation of the type:

$$A_Z = A_{Z,0} \times t_{UV}^{-d} \quad (13)$$

in which $A_{Z,0}$ stands for the activity parameter at t_{UV}=0 and d is the deactivation parameter which is a direct function of the rate of deactivation. As can be observed in Figure 8, the value of parameter d increases with the initial activity of the catalyst. The main cause of the deactivation of ZnO is photocorrosion, which consists in the partial dissolution of Zn and the collapse of the ZnO crystal structure as a result of the action of UV irradiation. Photocorrosion occurs via the following reactions [28,29]:

$$ZnO + 2h^+ + nH_2O \rightarrow Zn(OH)_n^{(2-n)+} + 1/2O_2 + nH^+ \quad (14)$$

$$ZnO + 2h^+ \rightarrow Zn^{2+} + 1/2O_2 \quad (15)$$

Several research groups have investigated how to reduce ZnO photocorrosion by means of procedures such as depositing silver [32-35], polyaniline monolayers [36], graphitic carbon [37], Nafion films [38] on the surface of the ZnO, or via hybridization of ZnO with C_{60} [29]. As mentioned above, reaction orders of over 1 could be caused by the phenomenon of catalytic deactivation. This can be easily visualised in Figure 9. This figure shows the theoretical variation of $C_{MB}/C_{MB,0}$ for experiments that yield the same initial reaction rate and different reaction orders. For a value of n over 1, the reaction rate diminishes with time with respect to that obtained for n=1. Catalyst deactivation leads to the same result.

Figure 10 confirms these findings. In this figure the values of ZnO losses after 12 hours of reaction and those of parameter d are plotted against the average value of reaction order for all the consecutive batch reactions performed with the catalysts. The losses of ZnO from photocorrosion, evaluated by the difference in catalyst weight, increase almost linearly with the average value of <n>, indicating that the value of this parameter depends on the extent of deactivation. The parallel behaviour between the values of d and ZnO losses confirms that loss of activity is due to photocorrosion. If the relation between the reaction order and the extent of deactivation is general, then the relationship between catalytic activity and deactivation rate observed for the catalysts of Figure 9 might be coincidence, since there is almost random variation between the values of n and A_Z, as can be seen in Table 4.

4. Conclusions

Zinc oxide nanostructures supported on stainless steel meshes that had been synthesized in a previous work (T.T. Vu, L. del Río, T. Valdés-Solís, and G. Marbán, Mater. Res. Bull., 47 (2012) 1577-1586) were tested for the photocatalytic decomposition of methylene blue under ultraviolet irradiation. A potential reaction rate equation was used to fit the results of the batch experiments. Because of the existence of different reaction orders and varying catalyst concentrations during the reaction, an activity parameter (A_C) was introduced to account for these variations. The best catalyst tested (S2-Ko) showed a catalytic activity higher than that of the reference material TiO_2 P25 (Degussa-Evonik). Its high activity is attributed to a higher quantum yield resulting from the small particle length of the ZnO deposited on the wire meshes. It has been proved that reaction orders of over 1 are due to catalysis deactivation caused by ZnO photocorrosion.

Acknowledgements

Tan T. Vu is grateful to CSIC for the award of a JAE predoc grant. The financial support for this research work provided by the Spanish MEC (CTQ2011-24776) is gratefully acknowledged. Funding through the FICYT Regional Project IB08-103 is also acknowledged.

Reference List

[1] D. Chatterjee and S. Dasgupta, Visible light induced photocatalytic degradation of organic pollutants, J. Photochem. Photobiol. C-Photochem. Rev., 6 (2005) 186-205.

[2] F. Akbal, Photocatalytic degradation of organic dyes in the presence of titanium dioxide under UV and solar light: Effect of operational parameters, Environ. Prog., 24 (2005) 317-322.

[3] W.S. Chiu, P.S. Khiew, M. Cloke, D. Isa, T.K. Tan, S. Radiman, R. bd-Shukor, M.A.A. Hamid, N.M. Huang, H.N. Lim, and C.H. Chia, Photocatalytic study of two-dimensional ZnO nanopellets in the decomposition of methylene blue, Chem. Eng. J., 158 (2010) 345-352.

[4] C. Lizama, J. Freer, J. Baeza, and H.D. Mansilla, Optimized photodegradation of Reactive Blue 19 on TiO2 and ZnO suspensions, Catal. Today, 76 (2002) 235-246.

[5] S. Sakthivel, B. Neppolian, M.V. Shankar, B. Arabindoo, M. Palanichamy, and V. Murugesan, Solar photocatalytic degradation of azo dye: comparison of photocatalytic efficiency of ZnO and TiO2, Sol. Energy Mater. Sol. Cells, 77 (2003) 65-82.

[6] L.E. Greene, M. Law, D.H. Tan, M. Montano, J. Goldberger, G. Somorjai, and P. Yang, General Route to Vertical ZnO Nanowire Arrays Using Textured ZnO Seeds, Nano Lett., 5 (2005) 1231-1236.

[7] C. Xu, P. Shin, L. Cao, and D. Gao, Preferential growth of long ZnO nanowire array and its application in dye-sensitized solar cells, J. Phys. Chem. C, 114 (2010) 125-129.

[8] S.H. Ko, D. Lee, H.W. Kang, K.H. Nam, J.Y. Yeo, S.J. Hong, C.P. Grigoropoulos, and H.J. Sung, Nanoforest of Hydrothermally Grown Hierarchical ZnO Nanowires for a High Efficiency Dye-Sensitized Solar Cell, Nano Lett., (2011) 666-671.

[9] Y. Feng, M. Zhang, M. Guo, and X. Wang, Studies on the PEG-Assisted Hydrothermal Synthesis and Growth Mechanism of ZnO Microrod and Mesoporous Microsphere Arrays on the Substrate, Crystal Growth & Design, 10 (2010) 1500-1507.

[10] P. Chen, L. Gu, X. Xue, Y. Song, L. Zhu, and X. Cao, Facile synthesis of highly uniform ZnO multipods as the supports of Au and Ag nanoparticles, Mater. Chem. Phys., 122 (2010) 41-48.

[11] W. Bai, K. Yu, Q. Zhang, X. Zhu, D. Peng, Z. Zhu, N. Dai, and Y. Sun, Large-scale synthesis of zinc oxide rose-like structures and their optical properties, Physica E, 40 (2008) 822-827.

[12] S. Baruah, C. Thanachayanont, and J. Dutta, Growth of ZnO nanowires on nonwoven polyethylene fibers, Sci. Technol. Adv. Mater., 9 (2008) 1-8.

[13] S. Baruah and J. Dutta, Hydrothermal growth of ZnO nanostructures, Sci. Technol. Adv. Mater., 10 (2009) 1-18.

[14] T.T. Vu, L. del Río, T. Valdés-Solís, and G. Marbán, Tailoring the synthesis of stainless steel wire mesh-supported ZnO, Mater. Res. Bull., 47 (2012) 1577-1586.

[15] G. Marbán, I. López, T. Valdés-Solís, and A.B. Fuertes, Highly active structured catalyst made up of mesoporous Co_3O_4 nanowires supported on a metal wire mesh for the preferential oxidation of CO, Int. J. Hydrogen Energy, 33 (2008) 6687-6695.

[16] G. Marbán, A. López, I. López, and T. Valdés-Solís, A highly active, selective and stable copper/cobalt-structured nanocatalyst for methanol decomposition, Appl. Catal. B: Environ., 99 (2010) 257-264.

[17] L. del Río and G. Marbán, Stainless steel wire mesh-supported potassium-doped cobalt oxide catalysts for the catalytic decomposition of nitrous oxide, Appl. Catal. B: Environ., 126 (2012) 39-46.

[18] S. Shao, P. Jia, S. Liu, and W. Bai, Stable field emission from rose-like zinc oxide nanostructures synthesized through a hydrothermal route, Mater. Lett., 62 (2008) 1200-1203.

[19] G. Marbán, T.T. Vu, and T. Valdés-Solís, Simple spectrum deconvolution technique to avoid the artifact induced by the hypsochromic shift masking the concentration of methylene blue analyzed by visible spectroscopy during photodegradation experiments, Appl. Catal. A: Gen., 402 (2011) 218-223.

[20] C.A.K. Gouvea, F. Wypych, S.G. Moraes, N. Duran, N. Nagata, and P. Peralta-Zamora, Semiconductor-assisted photocatalytic degradation of reactive dyes in aqueous solution, Chemosphere, 40 (2000) 433-440.

[21] N. Bouanimba, R. Zouaghi, N. Laid, and T. Sehili, Factors influencing the photocatalytic decolorization of Bromophenol blue in aqueous solution with different types of TiO_2 as photocatalysts, Desalination, 275 (2011) 224-230.

[22] J.M. Herrmann, Fundamentals and misconceptions in photocatalysis, J. Photochem. Photobiol. A Chem., 216 (2010) 85-93.

[23] M. Ahsan Habib, I.M.I. Ismail, A.J. Mahmood, and M. Rafique Ullah, Photocatalytic decolorization of Brilliant Golden Yellow in TiO_2 and ZnO suspensions, J. Saudi Chem. Soc., 16 (2011) 423-429.

[24] M. Muruganandham and M. Swaminathan, Solar photocatalytic degradation of a reactive azo dye in TiO_2-suspension, Sol. Energy Mater. Sol. Cells, 81 (2004) 439-457.

[25] Y. Zhang, J.C. Crittenden, D.W. Hand, and D.L. Perram, Fixed-bed photocatalysts for solar decontamination of water, Environ. Sci. Technol., 28 (1994) 435-442.

[26] D. Zhang, R. Qiu, L. Song, B. Eric, Y. Mo, and X. Huang, Role of oxygen active species in the photocatalytic degradation of phenol using polymer sensitized TiO_2 under visible light irradiation, J. Hazard. Mater., 163 (2009) 843-847.

[27] A.A. Khodja, T. Sehili, J.F. Pilichowski, and P. Boule, Photocatalytic degradation of 2-phenylphenol on TiO2 and ZnO in aqueous suspensions, J. Photochem. Photobiol. A Chem., 141 (2001) 231-239.

[28] A.L. Rudd, Photo-induced dissolution of zinc in alkaline solutions, Electrochim. Acta, 45 (2000) 1571-1579.

[29] H. Fu, T. Xu, S. Zhu, and Y. Zhu, Photocorrosion Inhibition and Enhancement of Photocatalytic Activity for ZnO via Hybridization with C_{60}, Environ. Sci. Technol., 42 (2008) 8064-8069.

[30] A. Mclaren, T. Valdés-Solís, G. Li, and S.C. Tsang, Shape and Size Effects of ZnO Nanocrystals on Photocatalytic Activity, J. Am. Chem. Soc., 131 (2009) 12540-12541.

[31] M. Öztas and M. Bedir, Thickness dependence of structural, electrical and optical properties of sprayed ZnO:Cu films, Thin Solid Films, 516 (2008) 1703-1709.

[32] C. Ren, B. Yang, M. Wu, J. Xu, Z. Fu, Y. lv, T. Guo, Y. Zhao, and C. Zhu, Synthesis of Ag/ZnO nanorods array with enhanced photocatalytic performance, J. Hazard. Mater., 182 (2010) 123-129.

[33] Z. Yang, P. Zhang, Y. Ding, Y. Jiang, Z. Long, and W. Dai, Facile synthesis of Ag/ZnO heterostructures assisted by UV irradiation: Highly photocatalytic property and enhanced photostability, Mater. Res. Bull., 46 (2011) 1625-1631.

[34] W. Xie, Y. Li, W. Sun, J. Huang, H. Xie, and X. Zhao, Surface modification of ZnO with Ag improves its photocatalytic efficiency and photostability, J. Photochem. Photobiol. A Chem., 216 (2010) 149-155.

[35] C. Tian, Q. Zhang, B. Jiang, G. Tian, and H. Fu, Glucose-mediated solution-solid route for easy synthesis of Ag/ZnO particles with superior photocatalytic activity and photostability, J. Alloy Compd., 509 (2011) 6935-6941.

[36] H. Zhang, R. Zong, and Y. Zhu, Photocorrosion inhibition and photoactivity enhancement for zinc oxide via hybridization with monolayer polyaniline, J. Phys. Chem. C, 113 (2009) 4605-4611.

[37] L.W. Zhang, H.Y. Cheng, R.L. Zong, and Y.F. Zhu, Photocorrosion suppression of ZnO nanoparticles via hybridization with graphite-like carbon and enhanced photocatalytic activity, J. Phys. Chem. C, 113 (2009) 2368-2374.

[38] J. Wang, P. Liu, S. Wang, W. Han, X. Wang, and X. Fu, Nanocrystalline zinc oxide in perfluorinated ionomer membranes: Preparation, characterization, and photocatalytic properties, J. Mol. Catal. A-Chem., 273 (2007) 21-25.

Captions to figures

Figure 1. Absorption spectra in the visible region for samples taken at different reaction times for some of the catalysts tested in this work. The deconvolution peaks were obtained by the technique described in [19].

Figure 2. Examples of the evolution of absorbance during the reaction for different peaks of the visible region (P1: methylene blue, P7-P8-P9: intermediate compounds) corresponding to catalysts with different activities.

Figure 3. Variation of the methylene blue concentration with reaction time for the experiments performed with reference catalyst TiO_2 P25. Inset: variation of the activity parameter, A_Z, with the catalyst weight.

Figure 4. Variation of the methylene blue concentration with reaction time for the different mesh-supported catalysts tested in this work. The dashed lines represent fittings to the potential equation (3).

Figure 5. A_Z and A_{MZ} values for the different catalysts tested in this work

Figure 6. Variation of A_Z with I_{101}/I_{002}, d_{XRD}, L, W, S, Y and S_g for the mesh-supported catalysts tested in this work

Figure 7. SEM microphotographs of the ZnO-meshes synthesised by the Ko and Bai method illustrating the effect of particle length on the photocatalytic activity

Figure 8. Variation of A_Z with reaction time for consecutive batch experiments performed with three different catalysts (stability experiments). The solid lines represent fittings to equation (13).

Figure 9. Theoretical curves of variation of $C_{MB}/C_{MB,0}$ with reaction time for experiments yielding the same initial reaction rate and different reaction orders.

Figure 10. Variation of ZnO mass losses after 12 hours of reaction and exponent d of equation (13) with the average reaction order obtained during the stability experiments.

Tables

Table 1. Variables used in this work for the synthesis of stainless steel wire mesh-supported ZnO

Method	Reference*	Synthesis			
		Zn precursor	Additives	Crystal growth	Air calcination
Xu [7]	S2-Xu	$Zn(NO_3)_2$	HMTA NH_4OH PEI	87ºC 3h	450ºC 30min
	S3-Xu				450ºC 30 min
Ko [8]	S2-Ko	$Zn(NO_3)_2$	HMTA PEI	95ºC 7h	350ºC 10 min
Feng [9]	S2-Feng	$Zn(NO_3)_2$	HMTA PEG	95ºC 4h	-
Chen [10]	S2-Chen-10	$Zn(CH_3COO)_2$	KOH	25ºC 10h	- -
Bai [11]	S0-Bai	$ZnCl_2$	NH_4OH	95ºC 5.5h	-
	S2-Bai				
	S2-Bai-C		NH_4OH PEI		350ºC 20 min
Shao [18]	S0-Shao	$ZnCl_2$	NH_4OH	95ºC 2h	-
	S2-Shao				

* S# prefix refers to the number of seeding stages

Table 2. Equations for evaluating C_{MB} and the activity parameter A_C under different circumstances

	C_{MB} (mg·L^{-1}) *	**A_C (mg$_C^{-1}$·L·min^{-1})**
C_c=constant; n=1	$C_{MB,0}\exp\left(-kC_{C,0}t\right)$ (4)	$\frac{k}{0.693}$ (9)
C_c≠constant; n=1	$C_{MB,0}\exp\left\{-kC_{C,0}\left(1/b\right)\ln\left[1/\left(1-bt\right)\right]\right\}$ (5)	$\frac{b}{C_{C,0}\left[1-\exp\left(-\frac{0.693\,b}{kC_{C,0}}\right)\right]}$ (10)
C_c=constant; n≠1	$\left[C_{MB,0}^{1-n}-\left(1-n\right)kC_{C,0}t\right]^{1/(1-n)}$ (6)	$\frac{k\left(1-n\right)}{C_{MB,0}^{1-n}\left(0.5^{1-n}-1\right)}$ (11)
C_c≠constant; n≠1	$\left\{C_{MB,0}^{1-n}-\left(1-n\right)kC_{C,0}\left(1/b\right)\ln\left[1/\left(1-bt\right)\right]\right\}^{1/(1-n)}$ (7)	$\frac{b}{C_{C,0}\left\{1-\exp\left[-\frac{C_{MB,0}^{1-n}\left(0.5^{1-n}-1\right)b}{kC_{C,0}(1-n)}\right]\right\}}$ (12)

* $C_{MB,0}$ = initial methylene blue concentration; $C_{C,0}$ = initial catalyst concentration (subscript C=Z on ZnO or TiO_2 mass basis; subscript C=MZ on mesh+ZnO mass basis)

Table 3. Gaussian parameters (mean wavelengths, λ_i, and standard deviations, σ_i) obtained with the deconvolution technique for the peaks corresponding to intermediate products (P7, P8 and P9)

Peak	**Catalyst**	**λ_i (nm)**	**σ_i (nm)**
P7	Mesh-supported ZnO	518.1 ± 4.8	40.3 ± 4.9
	TiO_2	530.9	42.0 ± 2.9
P8	Mesh-supported ZnO	611.5 ± 2.0	34.9 ± 2.7
	TiO_2	611.2	38.8 ± 5.7
P9	Mesh-supported ZnO	651.8 ± 3.2	17.5 ± 4.9
	TiO_2	648.4	19.1 ± 1.6

Table 4. Kinetic parameters for the methylene blue photodegradation obtained for the different catalysts analysed in this work

Reference	k (n^{th} order) * ($mg_{MB}^{1-n}\cdot mg_Z^{-1}\cdot L^n\cdot min^{-1}$)	n	A_Z * ($mg_Z^{-1}\cdot L\cdot min^{-1}$)	A_{MZ} ** ($mg_{MZ}^{-1}\cdot L\cdot min^{-1}$)
S2-Ko	6.1×10^{-5}	2.2	8.2×10^{-4}	3.5×10^{-5}
TiO_2	4.0×10^{-4}	1.0	5.8×10^{-4}	-
S2-Feng	5.6×10^{-5}	1.7	3.5×10^{-4}	1.0×10^{-5}
S0-Bai	1.9×10^{-6}	2.7	7.9×10^{-5}	5.5×10^{-6}
S2-Chen-10	2.5×10^{-5}	1.4	7.7×10^{-5}	1.4×10^{-5}
S0-Shao	2.8×10^{-8}	4.9	5.8×10^{-5}	4.1×10^{-6}
S2-Xu	4.5×10^{-5}	0.5	2.4×10^{-5}	4.5×10^{-6}
S2-Bai-C	1.3×10^{-5}	0.9	1.7×10^{-5}	4.6×10^{-6}
S3-Xu	2.8×10^{-5}	0.5	1.6×10^{-5}	3.5×10^{-6}
S2-Bai	2.7×10^{-12}	6.9	1.1×10^{-6}	3.1×10^{-7}
S2-Shao	4.1×10^{-9}	2.0	8.5×10^{-7}	2.4×10^{-7}

* Z: ZnO or TiO_2

** MZ: Mesh+ZnO

Figures

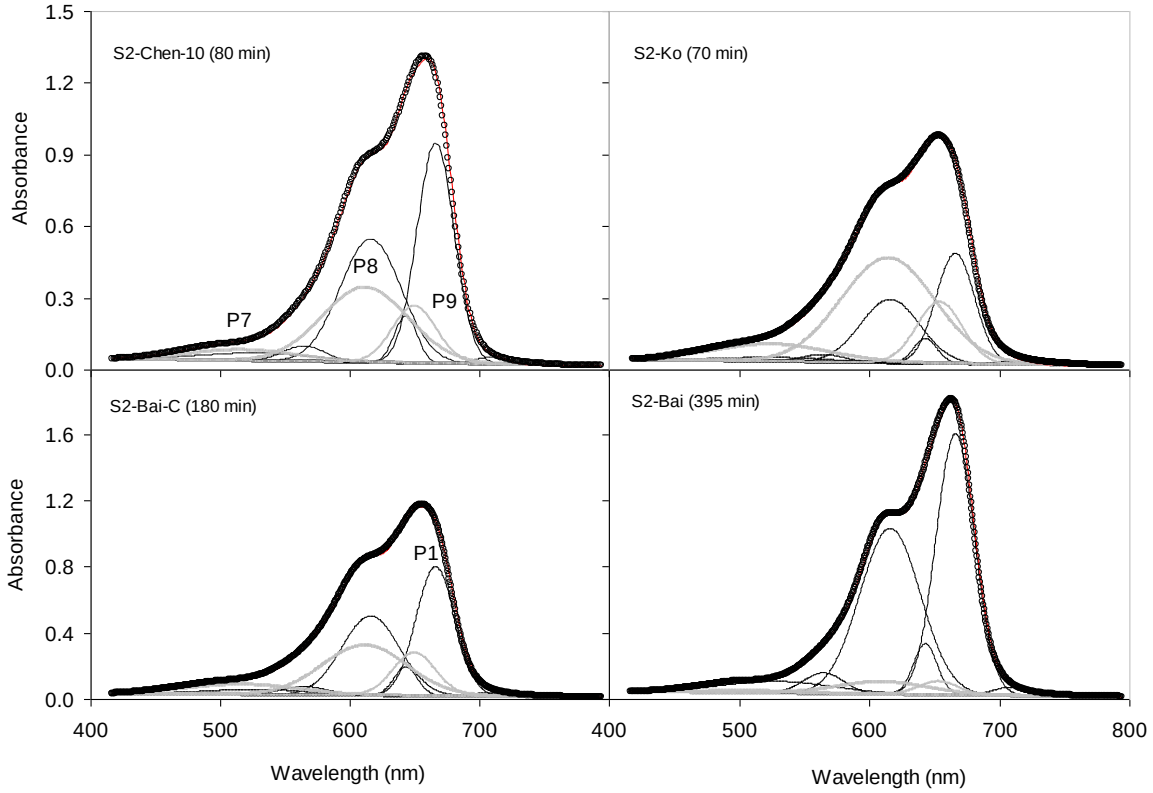

Figure 1

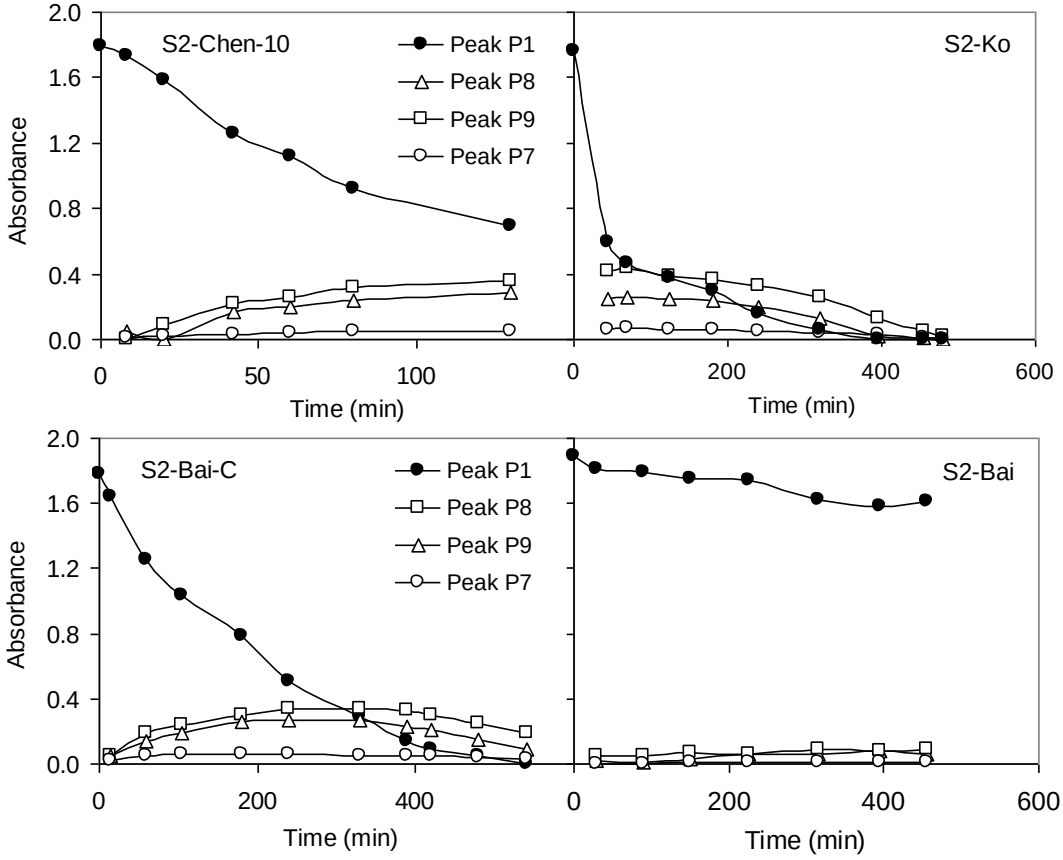
S2-Chen-10
Peak P1
Peak P8
Peak P9
Peak P7
S2-Ko
S2-Bai-C
S2-Bai
Absorbance
Time (min)
2.0
1.6
1.2
0.8
0.4
0.0
0
50
100
200
400
600

Figure 2

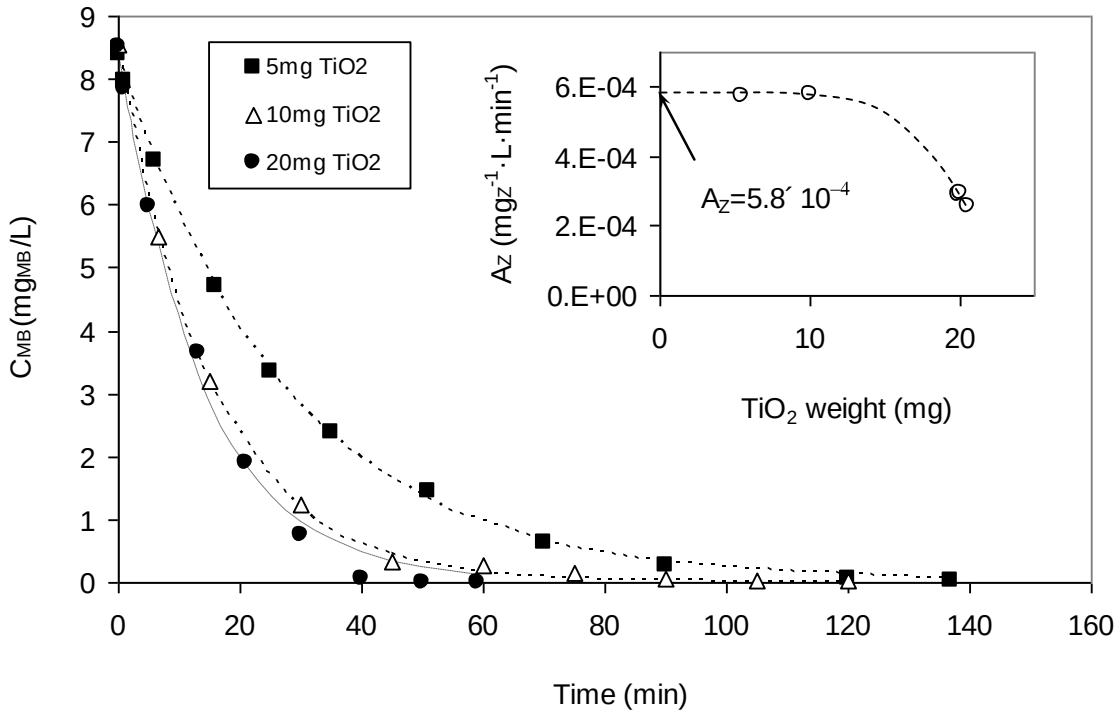
5mg TiO2
10mg TiO2
20mg TiO2
CMB (mgMB/L)
Time (min)
Az (mgz-1·L·min-1)
Az=5.8´ 10−4
TiO2 weight (mg)

Figure 3

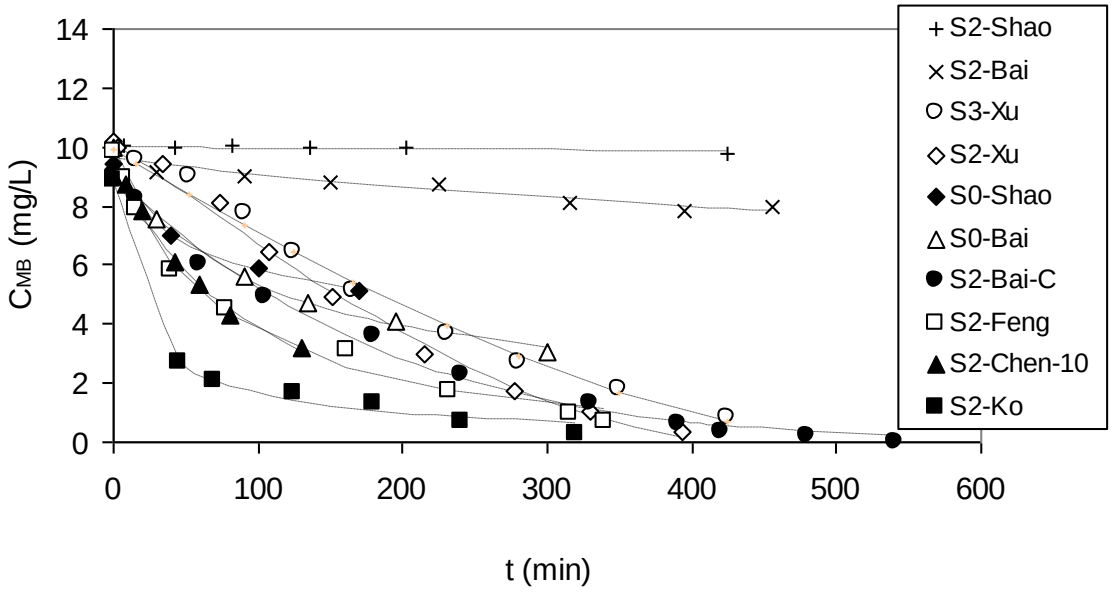
14
12
10
8
6
4
2
0
0
100
200
300
400
500
600
C_{MB} (mg/L)
t (min)
S2-Shao
S2-Bai
S3-Xu
S2-Xu
S0-Shao
S0-Bai
S2-Bai-C
S2-Feng
S2-Chen-10
S2-Ko

Figure 4

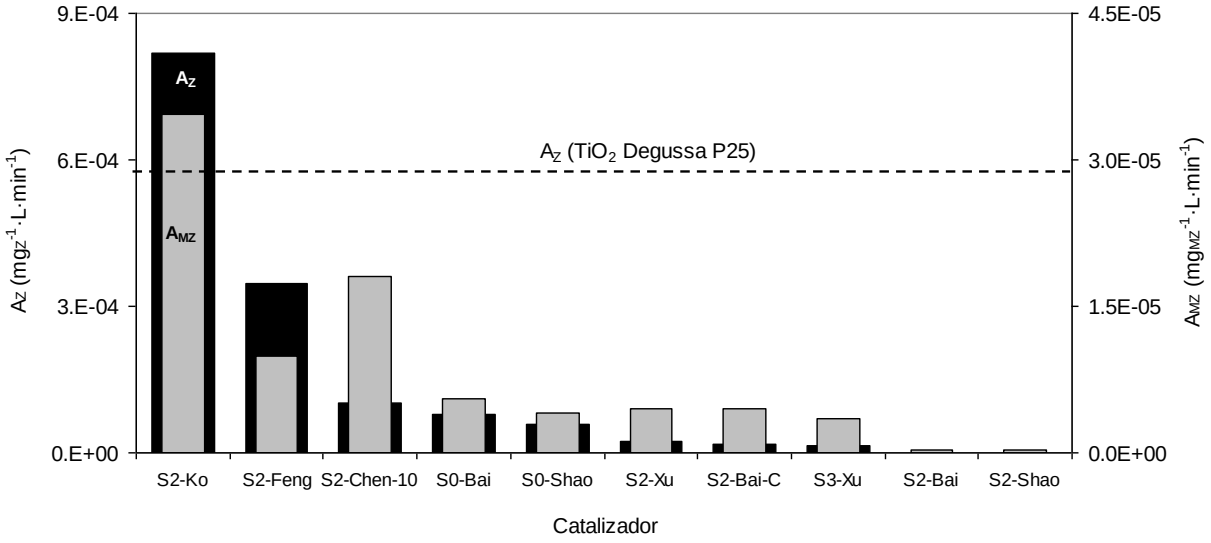
9.E-04
6.E-04
3.E-04
0.E+00
4.5E-05
3.0E-05
1.5E-05
0.0E+00
A_Z
A_{MZ}
A_Z (TiO_2 Degussa P25)
A_Z ($mg_Z^{-1}\cdot L\cdot min^{-1}$)
A_{MZ} ($mg_{MZ}^{-1}\cdot L\cdot min^{-1}$)
S2-Ko
S2-Feng
S2-Chen-10
S0-Bai
S0-Shao
S2-Xu
S2-Bai-C
S3-Xu
S2-Bai
S2-Shao
Catalizador

Figure 5

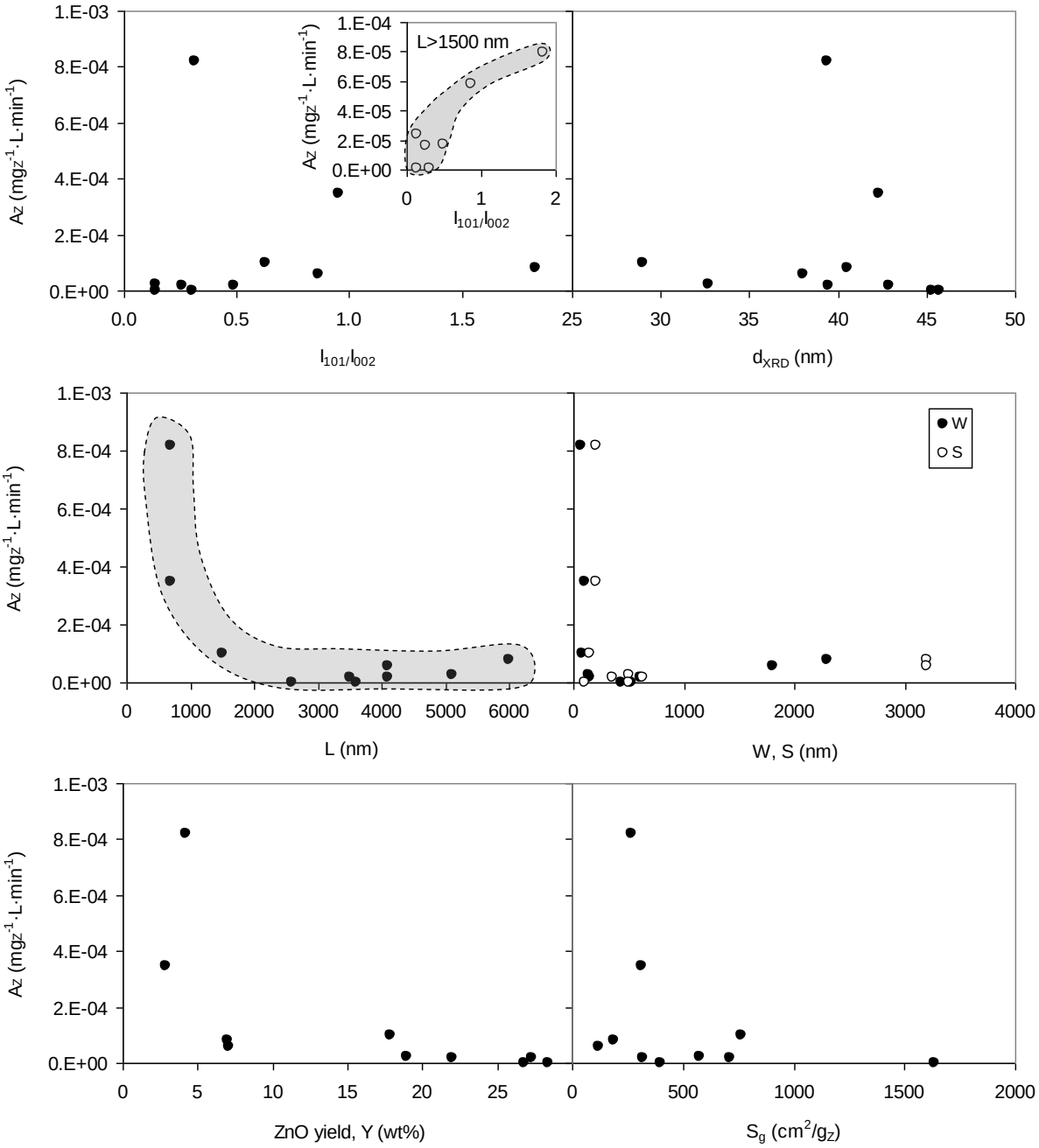
Az (mgz-1·L·min-1)
1.E-03
8.E-04
6.E-04
4.E-04
2.E-04
0.E+00
0.0
0.5
1.0
1.5
I101/I002
L>1500 nm
1.E-04
8.E-05
6.E-05
4.E-05
2.E-05
0.E+00
0
1
2
I101/I002
25
30
35
40
45
50
dXRD (nm)
0
1000
2000
3000
4000
5000
6000
L (nm)
W
S
0
1000
2000
3000
4000
W, S (nm)
0
5
10
15
20
25
ZnO yield, Y (wt%)
0
500
1000
1500
2000
Sg (cm2/gZ)

Figure 6

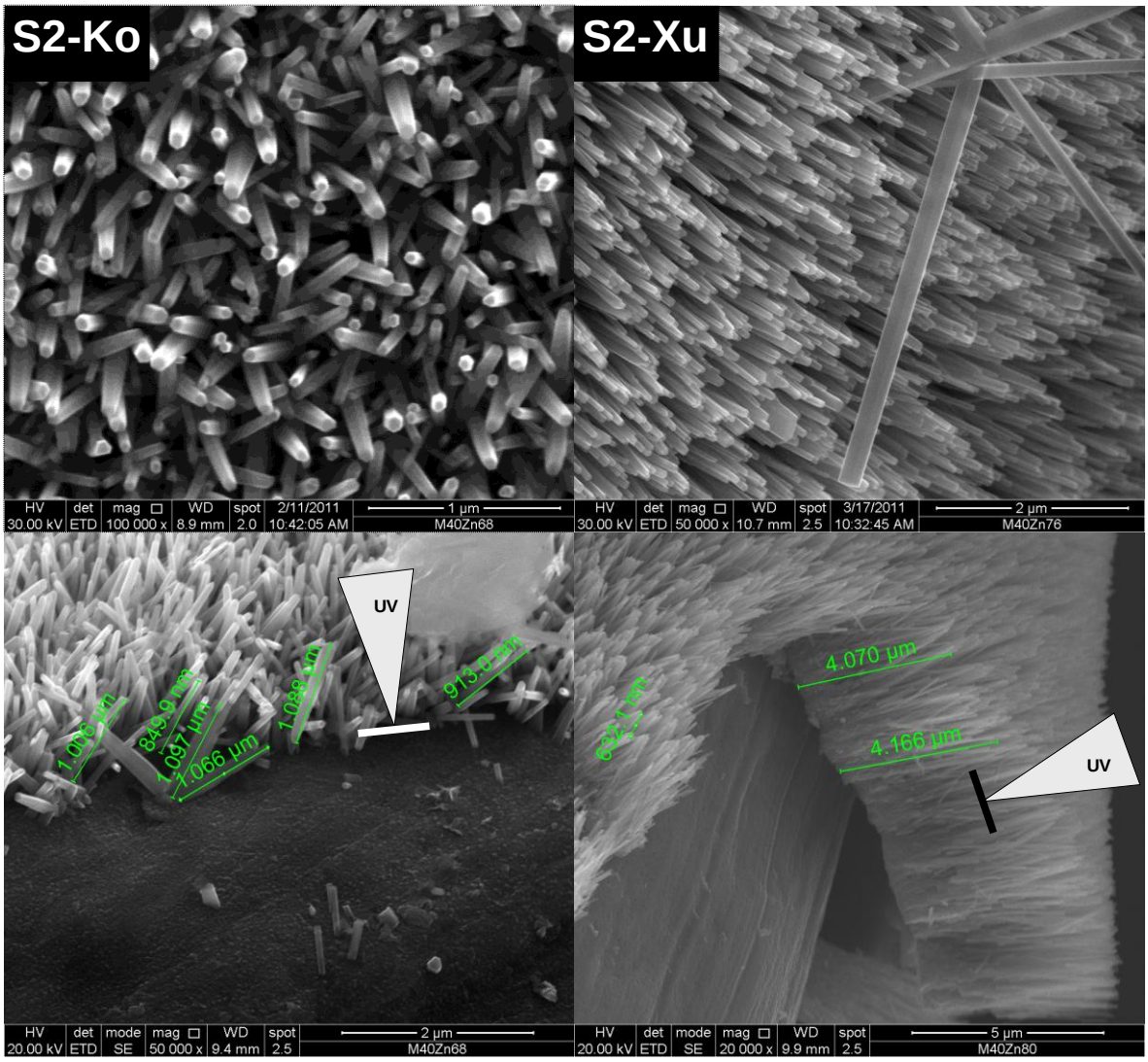
S2-Ko
S2-Xu
HV 30.00 kV | det ETD | mag 100 000 x | WD 8.9 mm | spot 2.0 | 2/11/2011 10:42:05 AM | 1 µm | M40Zn68
HV 30.00 kV | det ETD | mag 50 000 x | WD 10.7 mm | spot 2.5 | 3/17/2011 10:32:45 AM | 2 µm | M40Zn76
UV
1.066 µm
849.9 nm
1.097 µm
1.066 µm
1.028 µm
913.6 nm
HV 20.00 kV | det ETD | mode SE | mag 50 000 x | WD 9.4 mm | spot 2.5 | 2 µm | M40Zn68
4.070 µm
4.166 µm
UV
HV 20.00 kV | det ETD | mode SE | mag 20 000 x | WD 9.9 mm | spot 2.5 | 5 µm | M40Zn80

Figure 7

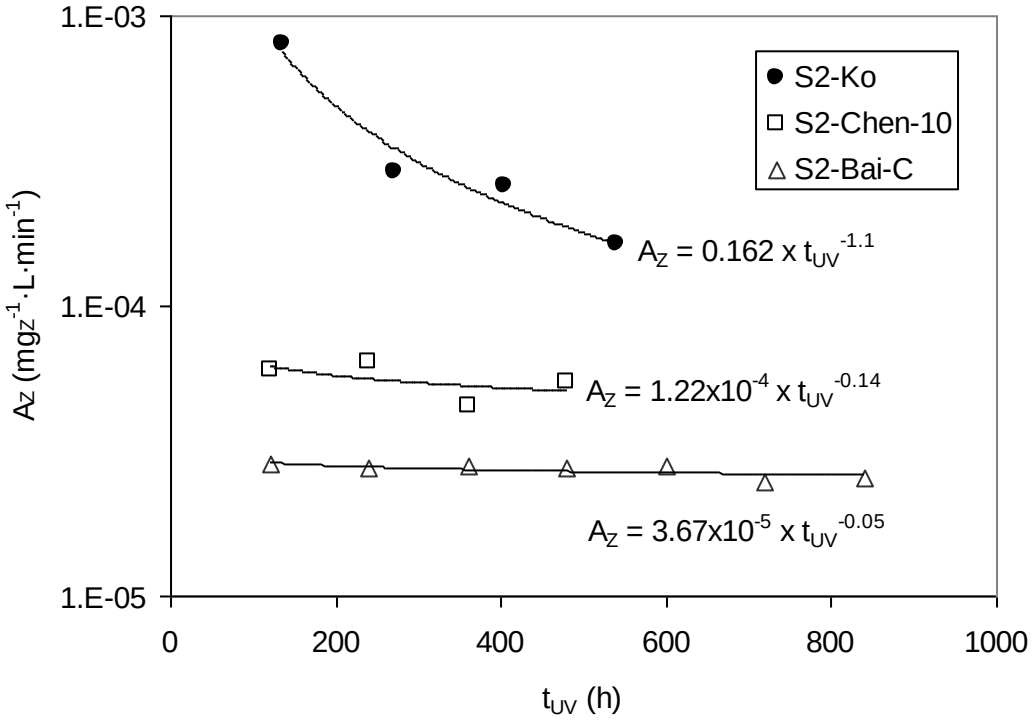
1.E-03
1.E-04
1.E-05
0
200
400
600
800
1000
A_Z (mgz^{-1}·L·min^{-1})
t_{UV} (h)
S2-Ko
S2-Chen-10
S2-Bai-C
$A_Z = 0.162 \times t_{UV}^{-1.1}$
$A_Z = 1.22\times10^{-4} \times t_{UV}^{-0.14}$
$A_Z = 3.67\times10^{-5} \times t_{UV}^{-0.05}$

Figure 8

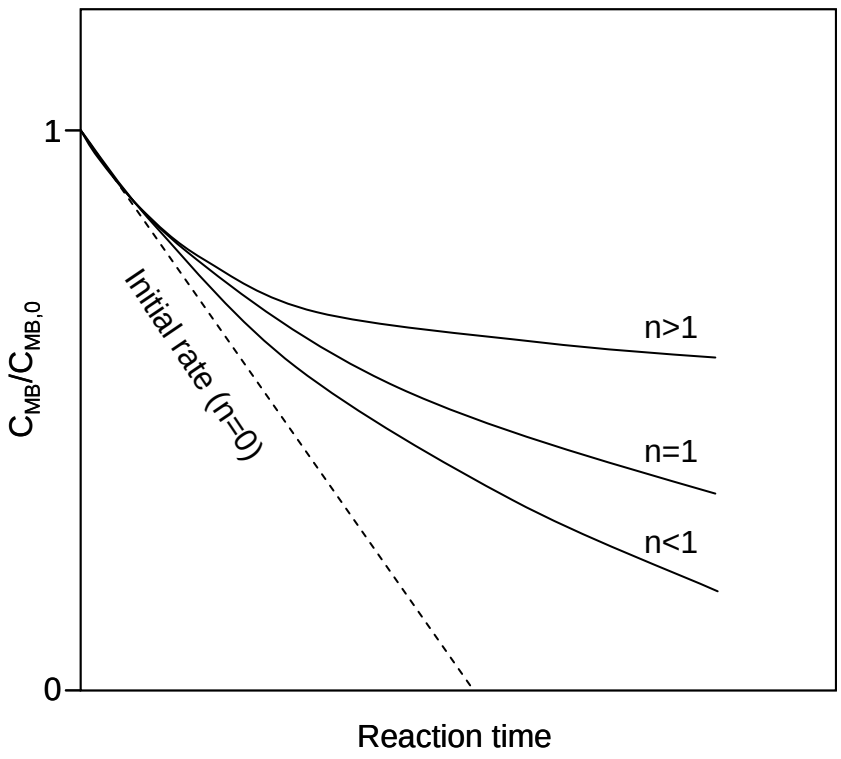

Figure 9

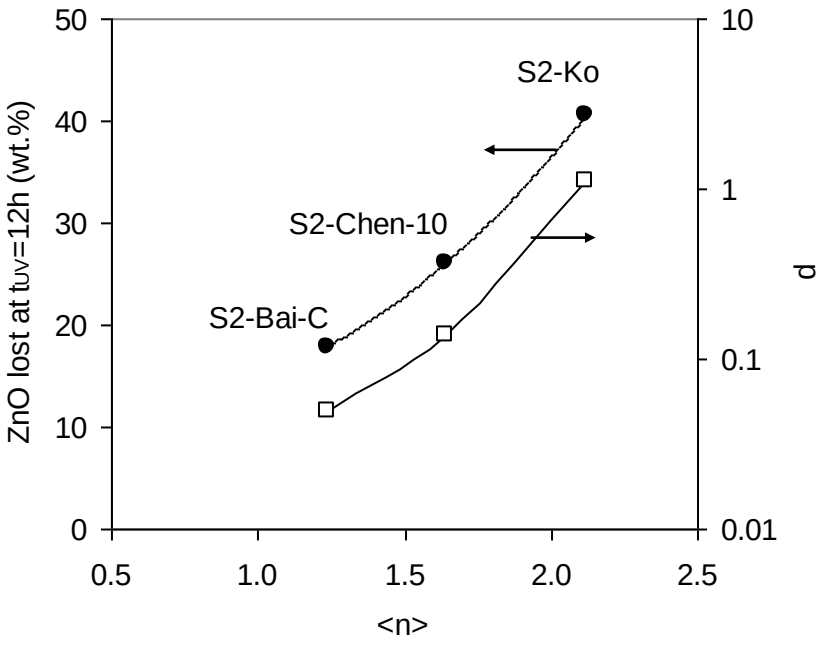
50
40
30
20
10
0
10
1
0.1
0.01
0.5
1.0
1.5
2.0
2.5
<n>
ZnO lost at tUV=12h (wt.%)
d
S2-Ko
S2-Chen-10
S2-Bai-C

Figure 10